

1 **Errors in Nanoparticle Growth Rates Inferred from**
2 **Measurements in Chemically Reacting Aerosol Systems**

3 Chenxi Li¹ and Peter H. McMurry¹

4 ¹Department of Mechanical Engineering, University of Minnesota, Minneapolis, MN, 55455, USA

5

6 *Correspondence to:* Chenxi Li (lixx3838@umn.edu)

7 **Abstract.** In systems where aerosols are being formed by chemical transformations, individual particles grow due
8 to the addition of molecular species. Efforts to improve our understanding of particle growth often focus on attempts
9 to reconcile observed growth rates with values calculated from models. However, because it is typically not possible
10 to measure the growth rates of individual particles in chemically reacting systems, they must be inferred from
11 measurements of aerosol properties such as size distributions, particle number concentrations, etc. This work discusses
12 errors in growth rates obtained using methods that are commonly employed for analyzing atmospheric data. We
13 analyze "data" obtained by simulating the formation of aerosols in a system where a single chemical species is formed
14 at a constant rate, R . We show that the maximum overestimation error in measured growth rates occurs for collision-
15 controlled nucleation in a single-component system in the absence of a pre-existing aerosol, wall losses, evaporation
16 or dilution, as this leads to the highest concentrations of nucleated particles. Those high concentrations lead to high
17 coagulation rates that cause the nucleation mode to grow faster than would be caused by vapor condensation alone.
18 We also show that preexisting particles, when coupled with evaporation, can significantly decrease the concentration
19 of nucleated particles. This can lead to decreased discrepancies between measured growth rate and true growth rate
20 by reducing coagulation between nucleated particles. However, as particle sink processes get stronger, measured
21 growth rates can potentially be lower than true particle growth rates. We briefly discuss nucleation scenarios where
22 the observed growth rate approaches zero while the true growth rate does not.

23

24 **1 Introduction**

25 Aerosol systems undergo transformations by processes that include coagulation, convection, deposition on surfaces,
26 source emissions, nucleation, growth, etc. The aerosol general dynamic equation (GDE) (Friedlander, 2000;Gelbard
27 and Seinfeld, 1979, 1980) describes the time rate of change of size-dependent particle concentration and composition
28 by such processes. Recent work has focused on understanding processes that affect growth rates of freshly nucleated
29 atmospheric nanoparticles (Smith et al., 2008;Smith et al., 2010;Riipinen et al., 2012;Hodshire et al., 2016;Kontkanen
30 et al., 2016;Tröstl et al., 2016).This is important because a particle's survival probability increases with growth rates
31 (McMurtry and Friedlander, 1979;Weber et al., 1997;Kerminen and Kulmala, 2002;Kuang et al., 2010). Nucleated
32 particles are more likely to form cloud condensation nuclei and affect climate when survival probabilities are high.

33 Following established conventions long used in modeling aerosol dynamics (Friedlander, 2000;Gelbard and Seinfeld,
34 1979, 1980), we define the particle "growth rate" as the net rate of change in diameter of individual particles due to
35 the addition or removal of molecular species. (If evaporation exceeds addition, the growth rate would be negative.)
36 While most work to date has focused on condensation and evaporation, chemical processes such as acid-base reactions,
37 organic salt formation, liquid phase reactions, and the accretion of two or more organic molecules to form a larger
38 compound having lower volatility may also contribute to growth (McMurtry and Wilson, 1982;Barsanti et al.,
39 2009;Riipinen et al., 2012;Lehtipalo 2014). In a chemically reacting system, the total diameter growth rate, GR , is
40 given by the sum of all such processes:

$$41 \frac{dd_p}{dt} = GR = GR_{\text{condensation/evaporation}} + GR_{\text{acid-base reactions}} + GR_{\text{accretion}} + GR_{\text{other}}. \quad (1)$$

42 The effect of growth on the aerosol distribution function is given by (Heisler and Friedlander, 1977):

$$43 \frac{\partial n}{\partial t} \Big|_{\text{Growth}} = -\frac{\partial}{\partial d_p} \left[n(d_p, t) \frac{dd_p}{dt} \right], \quad (2)$$

44 where the aerosol number distribution, $n(d_p, t)$ is defined such that the number concentration of particles between d_p
45 and $d_p + dd_p$ is equal to $n(d_p, t)dd_p$. Coagulation, including the coagulation of a molecular cluster with a larger
46 particle, can also lead to particle growth. It is worthwhile, however, to treat coagulation and growth separately. The
47 extent to which the coagulation of freshly nucleated molecular clusters contributes to measured growth rates can be
48 accurately determined only if the entire number distribution down to clusters of size 2 is accurately measured. In the
49 absence of such data, the contributions of cluster coagulation to growth could erroneously be attributed to vapor uptake.
50 Coagulation is accounted for with the coagulation integrals in the GDE and is a relatively well understood process
51 that can be described with reasonable confidence in models (Kürten et al., 2018;Chan and Mozurkewich, 2001).
52 Growth involves processes that are not well understood for chemically complex aerosol systems, such as the
53 atmosphere (Barsanti et al., 2009;Riipinen et al., 2012;Hodshire et al., 2016).

54 Progress towards understanding growth can be achieved through efforts to reconcile GRs that are observed
55 experimentally with values predicted by models. Such work requires that size- and time-dependent GRs be accurately
56 determined from observations. The literature includes many reports of observed GRs (Stolzenburg et al., 2005;Wang
57 et al., 2013;Riccobono, 2012;Tröstl et al., 2016), but uncertainties in reported values are typically not well understood.

58 Because it is usually not possible to measure the growth of individual particles as they undergo chemical
59 transformations, GRs are calculated indirectly using time-dependent observations of aerosol properties such as number
60 distributions or number concentrations larger than a given size. Those properties are typically affected by many
61 processes, some poorly understood, that can affect reported GRs to an unknown extent.

62 A variety of approaches have been used to extract GRs from observations. We refer to these values as GR_m , where the
63 subscript ‘m’ designates ‘measured’. Methods that we discuss include:

64 1. *Maximum Concentration Method* (Kulmala et al., 2012). During a nucleation event, particle concentrations in
65 a given size bin increase from their initial values, passing through a peak before they eventually decrease. This
66 technique involves noting the times that this maximum occurred in different size bins. The growth rate is
67 obtained by first fitting a linear function of particle diameter (corresponding to the size bins) vs. time, and then
68 calculating the slope of the fitted function.

69 2. *Appearance Time Method* (Lehtipalo 2014). This approach has been used to analyze data from condensation
70 particle counter (CPC) batteries (Riccobono, 2014), particle size magnifier (PSM) (Lehtipalo 2014), etc.. In
71 brief, GR_m is determined by the differences in concentration rise times (typically, either 5% or 50% of the
72 maximum) measured by the instruments with differing minimum detection sizes. A variation of this approach
73 was reported by Weber et al. (1997), who estimated growth rates from the observed time delay in measurements
74 of sulfuric acid vapor and particles measured with a condensation particle counter having a minimum
75 detectable size of about 3 nm.

76 3. *Log-normal Distribution Function Method* (Kulmala et al., 2012). Lognormal distributions are fit to the
77 growing mode of nucleated particles. GR_m is defined as the growth rate of the geometric mean size of these
78 distributions.

79 While these methods do not account for the effects of coagulation on measured changes in particle size, the literature
80 includes approaches that explicitly account for such effects (Lehtinen et al., 2004; Verheggen and Mozurkewich,
81 2006; Kuang et al., 2012; Pichelstorfer et al., 2017). Other work has applied the above techniques after confirming that
82 coagulation has an insignificant effect for the analyzed data (Kulmala et al., 2012) or explicitly accounting for the
83 effects of coagulation on GR_m (Stolzenburg et al., 2005; Lehtipalo et al., 2016).

84 This paper assesses errors of using GR_m calculated using techniques commonly employed in the literature to infer
85 particle growth rates. Our results are especially germane to GR of freshly nucleated particles ranging in size from
86 molecular clusters to about 40 nm. We use time-dependent distribution functions calculated numerically by McMurry
87 and Li (2017) as “data”. The only process contributing to the addition or removal of molecular species in that work
88 (i.e., to particle “growth rates” as is defined above) are condensation and evaporation. Because we understand this
89 model system perfectly, GR_{true} (i.e., the net growth rate due molecular exchange through condensation and evaporation)
90 can be calculated exactly. Errors in GR_m due to coagulation, wall deposition, scavenging by preexisting particles, or
91 dilution, are given by the difference between GR_{true} and GR_m . We do not examine errors associated with convection,
92 source emission, etc.

93 We are not the first to examine factors that cause GR_m to differ from GR_{true} . For example, Kontkanen (2016) used
94 simulations to show that discrepancies between measured growth rate based on appearance time (AGR) and growth
95 rate based on irreversible vapor condensation (CGR) can be significant. (Note GR_{true} used in this paper differs from
96 CGR in that GR_{true} also incorporates evaporation.) Our approach, which uses the non-dimensional formulation
97 described by McMurry and Li (2017), provides results that are generally applicable to nucleation and growth of a
98 single chemical species, so long as it is being produced by chemical transformations at a constant rate, R . We show
99 that the upper limit for overestimation of GR_{true} by GR_m occurs when nucleation takes place in the absence of pre-
100 existing aerosols and is collision-controlled (i.e., when evaporation rates from even the smallest clusters occur at rates
101 that are negligible relative to vapor condensation rates). Collision-controlled nucleation is an important limiting case
102 because there is growing evidence that atmospheric nucleation of sulfuric acid with stabilizing species is well-
103 described as a collision-controlled process (Almeida et al., 2013; Kürten et al., 2018; McMurry, 1980). Because cluster
104 evaporation, scavenging by preexisting aerosol, etc., all diminish the number of particles formed by nucleation,
105 overestimation of GR_{true} due to coagulation decreases as these processes gain in prominence. We do not explicitly
106 study the effect of growth by processes other than condensation or evaporation, such as heterogeneous growth
107 pathways that take place on or within existing particles. If such processes were to contribute significantly to growth,
108 they would lead to higher growth rates and therefore smaller relative errors in GR_m due to coagulation. Additionally,
109 we point out when particle sink processes consume nucleated particles at a fast rate (e.g. strong effects of dilution or
110 scavenging by preexisting particles), GR_m may not be used to estimate GR_{true} . Our results help to inform estimates of
111 uncertainties for systems with a single condensing species, or systems that can be modeled in a similar way to a single
112 species system (Kürten et al., 2018).

113 2 Methods

114 2.1 Discrete-sectional model

115 We utilize the dimensionless discrete-sectional model described by McMurry and Li (2017) to simulate evolution of
116 particle size distribution for a system with a single condensing species. We assume that the condensing species is
117 produced at a constant rate by gas phase reaction. Our code uses two hundred discrete bins and 250 sectional bins,
118 with a geometric volume amplification factor of 1.0718 for neighboring sections.

119 Physical processes that affect particle growth, including wall deposition, loss to pre-existing particles, cluster
120 evaporation and dilution, can be characterized by dimensionless parameters in this model. In the present study,
121 however, not all aforementioned processes are discussed. Our previous work shows that wall losses, scavenging by
122 preexisting particles and dilution have qualitatively similar effects on aerosol dynamics. Therefore, in this work we
123 focus on preexisting aerosols and dilution to illustrate factors that contribute to errors in measured growth rates, and
124 do not explicitly discuss wall deposition. A single dimensionless parameter, \sqrt{L} , is used to indicate the abundance of
125 preexisting particles, with larger \sqrt{L} representing higher concentration of preexisting particles (or, equivalently, a
126 slower rate at which the nucleating species is produced by chemical reaction). \sqrt{L} is calculated with the equation

127
$$\sqrt{L} = \frac{\frac{1}{4} \left(\frac{8k_b T}{\pi m_1} \right)^{1/2} A_{Fuchs}}{\sqrt{R \beta_{11 fm}}}, \quad (3)$$

128 where A_{Fuchs} is the Fuchs surface area concentration (Fuchs and Sutugin, 1971), k_b is the Boltzmann constant, m_1 is
 129 the mass of the monomer, R is the condensing species production rate, $\beta_{11 fm}$ is the monomer collision frequency
 130 function. The loss rate for particles containing k monomers is $\sqrt{L}/k^{1/2}$. This size dependence is included when
 131 solving the coupled differential equations for time-dependent cluster concentrations. Similarly, the dimensionless
 132 quantity M that characterizes dilution is given by the expression

133
$$M = \frac{Q_{dil}/V}{\sqrt{R \beta_{11 fm}}}, \quad (4)$$

134 where Q_{dil} is the dilution flow rate and V is the volume of the system. Note the fractional dilution loss is independent
 135 of particle size. In addition to loss to pre-existing particles and dilution, we consider the effect of cluster evaporation
 136 on particle growth with the assumption that evaporation follows the classical liquid droplet model. Two dimensionless
 137 parameters, E and Ω , are needed to fully describe the evaporation process. The dimensionless evaporation parameter,
 138 E , is proportional to the saturation vapor concentration of the nucleating species, while Ω is the dimensionless surface
 139 tension (Rao and McMurry, 1989; McMurry and Li, 2017). The evaporation rate for particles containing k monomers,
 140 E_k , is calculated with a discretized equation of the form:

141
$$E_k = E c_{1k} \exp \left[\frac{3}{2} \Omega \left(k^{\frac{2}{3}} - (k-1)^{\frac{2}{3}} \right) \right], \quad (5)$$

142 where $c(i, k)$ is the dimensionless collision frequency between a monomer and a particle containing k monomers. To
 143 simplify our discussion, Ω is fixed to be 16 throughout this work (a representative value for the surface tension of
 144 sulfuric acid aqueous solutions), while the value of E is varied.

145 The solution to the GDE for a constant rate system (R =constant) depends on dimensionless time, cluster size and the
 146 dimensionless variables \sqrt{L} , M , E , Ω , etc., but is independent of the rate at which condensing vapor is produced by
 147 chemical reaction. That rate is required to transform the computed nondimensional solutions to dimensional results
 148 using simple multiplicative expressions given by McMurry and Li (2017):

149
$$N_k = \left(\frac{R}{\beta_{11 fm}} \right)^{1/2} \tilde{N}_k; t = \left(\frac{1}{R \beta_{11 fm}} \right)^{1/2} \tau; d_p = (v_1^{1/3}) \tilde{d}_p. \quad (6)$$

150 In the above equations, \tilde{N}_k is the dimensionless concentration of particle containing k monomers, τ is the
 151 dimensionless time, \tilde{d}_p is the dimensionless particle size and v_1 is the monomer volume. Assuming a monomer
 152 volume of $1.62 \times 10^{-22} \text{ cm}^3$ (volume of one sulfuric acid plus one dimethylamine molecule with a density of
 153 1.47 g/cm^3), $\tilde{d}_p = 30$ would be equivalent to a dimensional particle size of 16.4 nm.

154 **2.2 Evaluation of measured growth rate (GR_m)**

155 At time t_1 and t_2 , if two particle sizes $d_{p,t1}$ and $d_{p,t2}$ are used to represent the particle size distribution, the ‘measured’
 156 growth rate can be calculated using the following equation as a first order approximation

$$157 GR_m\left(\frac{d_{p,t1}+d_{p,t2}}{2}, \frac{t_2+t_1}{2}\right) = \frac{d_{p,t2}-d_{p,t1}}{t_2-t_1}. \quad (7)$$

158 If d_{p,t_i} is available for a time series $\{t_i\}_{i=1,2,\dots}$, growth rate can also be obtained by derivatizing a fitting function
 159 $d_p = d_p(t)$ to obtain growth rate at any time t_a :

$$160 GR_m(d_p, t_a) = \left. \frac{dd_p(t)}{dt} \right|_{t=t_a}. \quad (8)$$

161 To implement Eq. (7) or (8), it is necessary to choose a particle size that is representative of the particle size distribution
 162 at a given time. The choice of this representative size varies among publications and can depend on the types of
 163 available data. Based on previous studies (Kulmala et al., 2012;Lehtipalo 2014;Stolzenburg et al., 2005;Yli-Juuti,
 164 2011), we have selected four representative sizes for discussion: $\tilde{d}_{p,mode}$, $\tilde{d}_{p,sr100}$, $\tilde{d}_{p,sr50}$ and $\tilde{d}_{p,tot50}$. At a given
 165 time τ , $\tilde{d}_{p,mode}$ is the particle size at which $d\tilde{N}(\tau)/d\log_{10}\tilde{d}_p$ reaches its local maximum. If the shape of the mode is
 166 log-normal, $\tilde{d}_{p,mode}$ is equal to the geometric mean of the distribution. As suggested by Kulmala et al. (Kulmala et
 167 al., 2012), the ‘log-normal distribution method’ involves calculating growth rates from observed time-dependent
 168 trends of $\tilde{d}_{p,mode}$. The ‘maximum concentration method’ is based on the time when particles in a given size bin,
 169 $\tilde{d}_{p,sr100}$, pass through their maximum (100%) concentration (Lehtinen and Kulmala, 2003). The ‘appearance time’
 170 method is based on the time when particle concentrations in a bin, $\tilde{d}_{p,sr50}$, pass through a specified percentage of its
 171 maximum (we have used 50%). Growth rates are sometimes based on total concentrations of particles larger than a
 172 specified size. We refer to the particle size above which the total number concentration of particles reaches 50% of its
 173 maximum value as $\tilde{d}_{p,tot50}$. This approach is especially useful when measurements are carried out with a battery of
 174 CPCs having differing cutoff sizes. For simplicity, in this paper we assume that CPC detection efficiencies increase
 175 from 0% to 100% at a given cutoff size. In practice, measured size-dependent detection efficiencies are typically used
 176 when analyzing CPC battery data. Figure 1 shows the location of these representative sizes at $\tau = 20, 60, 100$ for two
 177 nucleation scenarios in the absence of preexisting particles. $\tilde{d}_{p,mode}$, $\tilde{d}_{p,sr100}$, $\tilde{d}_{p,sr50}$ and $\tilde{d}_{p,tot50}$ are marked as
 178 points, with their y-coordinates representing particle concentrations at corresponding sizes.

179 As will be shown later, values of GR_m obtained with $\tilde{d}_{p,mode}$, $\tilde{d}_{p,sr100}$, $\tilde{d}_{p,sr50}$ or $\tilde{d}_{p,tot50}$ are not equal. To
 180 differentiate these cases, GR_m are notated as $GR_{m,mode}$, $GR_{m,sr100}$, $GR_{m,sr50}$ and $GR_{m,tot50}$ accordingly.

181 **2.3 Evaluation of true growth rate (GR_{true})**

182 The true growth rate (GR_{true}) defined in this paper follows the Lagrangian approach (Olenius et al., 2014), i.e. tracking
 183 the volume change of individual particles, and only include molecular species exchange by condensation and
 184 evaporation. It is calculated with the following expression:

$$185 GR_{true} = \frac{d\tilde{d}_p}{d\tau} = \frac{2}{\pi\tilde{d}_p^2} \frac{d\tilde{V}}{d\tau} = \frac{2}{\pi\tilde{d}_p^2} \cdot \frac{\tilde{V} + c(i,k)\tilde{N}_1 \cdot d\tau - E_k \cdot d\tau - \tilde{V}}{d\tau} = \frac{2(c(i,k)\tilde{N}_1 - E_k)}{\pi\tilde{d}_p^2}, \quad (9)$$

186 where \tilde{d}_p is the representative size, \tilde{N}_1 is the concentration of monomers, and E_k is the particle evaporation rate given
187 by Eq. (5).

188 If evaporation is negligible ($E = 0$) and \tilde{N}_1 is constant, Eq. (9) leads to a higher growth rate for smaller particles,
189 mainly because of the increased monomer collision frequency relative to particle size (Tröstl et al., 2016). Throughout
190 this work Eq. (9) is used to evaluate true particle growth rate. Note GR_{true} is calculated from dimensionless size and
191 time, and is therefore dimensionless. Since we focus on relative values of true and measured growth rates, our
192 conclusions are unaffected by the dimensionality of GR . However, dimensionless growth rates can be converted to
193 dimensional values with Eq. (6).

194 **3. Results and discussion**

195 **3.1 Error of using $GR_{m,mode}$ as GR_{true}**

196 As mode diameter ($\tilde{d}_{p,mode}$) is often employed to derive particle growth rate, in this section we discuss the error of
197 using $GR_{m,mode}$ as a substitute for GR_{true} in the absence of preexisting particles. The effect of preexisting particles is
198 discussed in Sect. 3.3.

199 Both condensation and coagulation lead to growth of $\tilde{d}_{p,mode}$. To understand their relative importance, we attribute
200 $GR_{m,mode}$ to three processes: monomer condensation minus evaporation (GR_{true}), coagulation of the mode with clusters
201 ($GR_{m,cluster}$) and self-coagulation of the mode ($GR_{m,self}$). The latter two processes are the main causes of the discrepancy
202 between $GR_{m,mode}$ and GR_{true} . To evaluate $GR_{m,cluster}$ and $GR_{m,self}$, the range of ‘clusters’ and ‘mode’ are defined as
203 illustrated in Fig. 1 by the two shaded regions at $\tau = 100$: clusters (beige) and nucleation mode (light blue). Clusters
204 and nucleation mode are separated by $\tilde{d}_{p,min}$, where $d\tilde{N}/d\log_{10}\tilde{d}_p$ is at a local minimum. Stolzenburg et al.(2005)
205 assumed the nucleation mode is lognormal and calculated GR_{true} and $GR_{m,self}$ with the method of moments. In this
206 work, since the mode for collision-controlled nucleation deviates significantly from log-normal (see Fig. 1a), no
207 assumption regarding the shape of the nucleation mode is made. Instead, $GR_{m,cluster}$, $GR_{m,self}$ are calculated with the
208 first order numerical approximation method outlined in Appendix A.

209 The calculation results are summarized by Fig. 2. We first consider collision-controlled nucleation ($E=0$). For this
210 nucleation scenario, Fig. 2a shows $\tilde{d}_{p,mode}$ on the left y axis and growth rate values on the right. A third order
211 polynomial is used for fitting $\tilde{d}_{p,mode} = \tilde{d}_{p,mode}(\tau)$ and is plotted as a solid black line. Differentiating the fitted
212 polynomial with respect to time gives the value of $GR_{m,mode}$. It is clear that GR_{true} only accounts for a small fraction
213 (17%-20%) of GR_m and is on par with contribution of $GR_{m,cluster}$ (15%-22%). Self-coagulation is the major contributor
214 (62%-78%) to GR_m . Thus, using $GR_{m,mode}$ as a substitute for GR_{true} leads to an overestimation by as much as a factor
215 about 6. We believe collision-controlled nucleation ($E=0$) in the absence of other particle loss mechanisms such as
216 wall deposition ($W=0$) and scavenging by pre-existing particles ($\sqrt{L}=0$) provides an upper limit for overestimation of
217 GR_{true} for a constant rate system ($R=\text{constant}$). This is because these conditions lead to the maximum number of
218 particles that can be produced by nucleation. High concentrations lead to high coagulation rates, and it is coagulation

219 that is primarily responsible for errors in GR_m . Furthermore, as is discussed below, the absence of evaporation and
220 scavenging by nucleated particles keeps monomer concentrations low relative to values achieved when $E \neq 0$ (see Fig.
221 2a). Low monomer concentrations reduce the value of GR_{true} , thereby increasing relative errors in GR_m .

222 Distinctive features of particle growth emerge when cluster evaporation is included by setting $E = 1 \times 10^{-3}$. Figure
223 2b shows results for this nucleation scenario. Most noticeably, particles grow considerably faster at early stages of
224 simulation. This occurs because evaporation depletes clusters and correspondingly increases monomer concentration.
225 In the absence of pre-existing particles, monomer concentration accumulates until the supersaturation is high enough
226 for nucleation to take place (see figure 2c). The accumulated monomers then rapidly condense on the nucleated
227 particles, leading to the rapid particle growth shown in figure 2b. To capture this rapid growth, two third-order
228 polynomials are used to fit $\tilde{d}_{p,mode}$ values for $\tau < 40$ and $\tau > 35$ respectively, with an overlapping region for $35 <$
229 $\tau < 40$. Furthermore, in comparison to collision-controlled nucleation, contribution of $GR_{m,cluster}$ to $GR_{m,mode}$ becomes
230 negligible, due to decreased cluster concentration by evaporation. For $\tau > 30$, GR_{true} accounts for about 40%-55% of
231 $GR_{m,mode}$, larger than that of collision-controlled nucleation; for $\tau < 25$, GR_{true} almost entirely accounts for $GR_{m,mode}$
232 and even exceeds $GR_{m,mode}$ at the very beginning of the nucleation. $GR_{true}/GR_{m,mode} > 1$ indicates a rapidly forming
233 nucleation mode, where freshly nucleated particles enter the mode and skew the mode distribution toward smaller
234 sizes, slowing down the shift of the mode peak towards larger values.

235 Increase of $GR_{true}/GR_{m,mode}$ by evaporation is explained by the elevated monomer concentration due to particle
236 volatility and the smaller number of particles formed by nucleation: the former increases GR_{true} , and the latter decreases
237 $GR_{m,self}$ and $GR_{m,cluster}$. Figure 2c plots monomer concentration \tilde{N}_1 as a function of time for several values of E .
238 Noticeably, monomer concentration elevates with E since higher cluster evaporation rates require higher monomer
239 concentrations (i.e., higher supersaturation) to overcome the energy barrier of nucleation. Once nucleation takes place,
240 high monomer concentration leads to rapid nanoparticle growth rates.

241 Figure 2d shows $GR_{true}/GR_{m,mode}$ at $\tau = 30, 50, 100, 150$ for several E values. At a given time, $GR_{true}/GR_{m,mode}$ clearly
242 increases with E : when evaporation rates are not negligible (i.e., $E \neq 0$), $GR_{m,mode}$ is closer to GR_{true} than occurs when
243 $E=0$. Again, this is because the elevated monomer concentrations increase GR_{true} and the lowered concentrations of
244 clusters and nucleated particles decrease $GR_{m,cluster}$ and $GR_{m,self}$. As E approaches 0, the value of $GR_{true}/GR_{m,mode}$
245 converges to that of the collision-controlled nucleation (~ 0.2). One data point, corresponding to $E = 5 \times 10^{-3}$ and
246 $\tau = 30$, with a value of 1.8, is not shown in Fig. 2d. It has a value significantly greater than unity because of the large
247 quantities of nucleated particles entering the mode, skewing the mode peak toward smaller sizes.

248 3.2 Comparison of representative sizes

249 In this section we examine how observed growth rate depends on the choice of a representative size. The application
250 of $GR_{m,mode}$ to deduce GR_{true} , though convenient in practice, depends on the existence of a nucleation mode. However,
251 the nucleation mode is usually not well defined in the early stage of nucleation. In contrast, growth rate based on other
252 representative sizes ($\tilde{d}_{p,sr50}$, $\tilde{d}_{p,sr100}$ and $\tilde{d}_{p,tot50}$) are not dependent on mode formation and are available for all
253 particle sizes. In light of this, $GR_{m,sr100}$, $GR_{m,sr50}$, $GR_{m,tot50}$ have often been employed to describe the growth rate of

254 small particles (<5nm). The effects of pre-existing particles are neglected in this section (i.e., $\sqrt{L} = 0$) but are
255 discussed in Sect. 3.3.

256 For collision-controlled nucleation, $\tilde{d}_{p,mode}$, $\tilde{d}_{p,sr50}$, $\tilde{d}_{p,sr100}$, $\tilde{d}_{p,tot50}$ are plotted as functions of time in Fig. 3a. The
257 magnitude of the representative sizes follow $\tilde{d}_{p,mode} < \tilde{d}_{p,bin100} < \tilde{d}_{p,tot50} < \tilde{d}_{p,bin50}$, as was previously illustrated in
258 Fig. 1a. $\tilde{d}_{p,mode} < \tilde{d}_{p,bin100}$ indicates that a certain measurement bin first reaches its maximum concentration and
259 becomes a local maximum at a later time. This is true for collision-controlled nucleation with a decreasing peak
260 concentration but is not necessarily true for other nucleation scenarios. The observed growth rate (i.e. slope of curves
261 in Fig. 3a) are shown in Fig. 3b as a function of representative size, with a clear relationship $GR_{m,mode} < GR_{m,sr100}$
262 $< GR_{m,tot50} < GR_{m,sr50}$. Note that $GR_{m,mode}$ is not available for small sizes, indicating the nucleation mode is yet to form
263 at the early stage of nucleation. Figure 3c shows GR_{true}/GR_m as a function of representative size, with GR_{true} calculated
264 with Eq. (9). Clearly GR_{true} accounts for the highest percentage of GR_m at the start of nucleation. This is partly due
265 to higher monomer concentrations (see red solid curve in Fig. 2c) and partly due to Eq. (9) that leads to higher true
266 growth rate for smaller particles: the addition of a monomer leads to a bigger absolute as well as fractional diameter
267 growth for small particles.

268 Figure 3d-3f are counterparts of Fig. 3a-3c, but with evaporation constant E set to 1×10^{-3} . Figure 3d show that $\tilde{d}_{p,sr50}$
269 and $\tilde{d}_{p,tot50}$ increase relatively slowly at the start of the simulation (see the amplified figure at the lower right corner
270 of Fig. 3d; for reference, the dimensionless sizes of monomer, dimer and trimer are 1.24, 1.56 and 1.79 respectively).
271 Subsequently, a marked change slope of the $\tilde{d}_p = \tilde{d}_p(\tau)$ curve is observed, indicating accelerated particle growth.
272 This reflects that nucleation occurs with a burst of particle formation following a process of monomer and cluster
273 accumulation. The slow growth of the smallest clusters is an indication that the accumulation process is slow due to
274 the strength of the Kelvin effect.

275 Figure 3e shows GR_m obtained by curve fitting after the nucleation burst and Fig. 3f shows the corresponding
276 GR_{true}/GR_m values. Different from collision-controlled nucleation, there is a sharp rise of GR_{true}/GR_m value at the start
277 of nucleation. This is due to the sharp decrease of the evaporation term in Eq. (9), causing the value of GR_{true} to
278 increase sharply. As nucleation progresses, the ratio of GR_{true} to $GR_{m,sr100}$, $GR_{m,tot50}$ and $GR_{m,sr50}$ comes close to 1,
279 with $GR_{m,mode}$ not yet available. Eventually, GR_{true}/GR_m for all representative sizes decreases and fall into the range
280 of 30%-50%, with GR_m^{mode} giving the best estimate of GR_{true} . Note the value of $GR_{true}/GR_{m,mode}$ significantly
281 exceeds unity for $\tilde{d}_p \in [5, 11]$ due to the distortion of the mode toward smaller sizes by high flux of freshly nucleated
282 particles into the mode.

283 3.3 Effect of pre-existing particles

284 Pre-existing particles act as particle sinks to decrease the intensity of nucleation. Similarly, in chamber experiments,
285 though loss to pre-existing particles is often eliminated by using air that is initially particle-free, loss of particles to
286 chamber walls is inevitable. Since wall loss and loss to preexisting particles have qualitatively similar effect on
287 nucleation (McMurry and Li, 2017), we selectively examine the effect of preexisting particles on growth rate

288 measurements to qualitatively illustrate the effects of all of these processes. To probe the initial stage of nucleation,
289 we use $\tilde{d}_{p,bin50}$ as the basis for our analysis, with a comparison of representative sizes presented at the end of this
290 section. As to the magnitude of \sqrt{L} , we choose $\sqrt{L} \in [0,0.3]$ based on previous work. It was shown in Fig. 2b in
291 McMurry and Li (2017) that as \sqrt{L} exceeds 0.1, particle size distributions begin to deviate discernably from the
292 collision-controlled case. In addition, $\sqrt{L} \approx 0.2$ was observed in the ANARChE field campaign carried out in Atlanta
293 for nucleation events with sulfuric acid as the major nucleating species (Kuang et al., 2010).

294 The influence of preexisting particles on the discrepancy between true and measured growth rate (GR_{true}/GR_m) is
295 twofold. On one hand, preexisting particles can decrease monomer concentration which leads to a smaller GR_{true} . On
296 the other hand, preexisting particles reduce coagulation by scavenging nucleated particles, which could result in a
297 narrower gap between GR_{true} and GR_m . Therefore, the response of GR_{true}/GR_m to \sqrt{L} depends on the relative magnitude
298 of these two competing effects. Figure 4a shows $\tilde{d}_{p,sr50}$ as a function of time for several \sqrt{L} values and Fig. 4b displays
299 the corresponding GR_{true}/GR_m values. It can be seen that GR_{true}/GR_m positively correlates with \sqrt{L} , indicating
300 preexisting particles are more effective in removing nucleated particles than reducing monomer concentrations. In
301 fact, as further demonstrated by Fig. 4c, monomer concentrations (leftmost point of all the curves) are barely affected:
302 scavenging of monomers by preexisting particles are offset by less condensation of monomers onto nucleated particles.
303 Note that for the range of \sqrt{L} values examined, the presence of preexisting particles alter GR_{true}/GR_m values by no
304 more than 50% for collision-controlled nucleation.

305 Figures 4d-4f show the same quantities as are shown in Fig. 4a-4c, but with E set to 1×10^{-3} instead of zero. In
306 contrast to collision-controlled nucleation, pre-existing particles significantly affect the nucleation process when
307 cluster evaporation is taken into account. As \sqrt{L} increases, Fig. 4e shows GR_{true}/GR_m converges to a value slightly
308 larger than unity. This indicates that the contribution of coagulation to measured growth rate approaches zero as \sqrt{L}
309 becomes large; or equivalently, the concentration of nucleated particles is severely decreased by pre-existing particles.
310 Values of $GR_{true}/GR_{m,sr50}$ slightly exceed unity for large sizes (Fig. 4f) due to the slightly higher condensational growth
311 rates of smaller particles in the nucleation mode. This shifts values of $\tilde{d}_{p,sr50}$ towards smaller sizes than would occur
312 if all particles were to grow at the same rate, causing $GR_{m,sr50}$ to be smaller than GR_{true} .

313 The decrease of nucleated particle concentration is further demonstrated in Fig. 4f. From $\sqrt{L} = 0$ to $\sqrt{L} = 0.3$, the
314 peak concentration of nucleated particles dropped by about three orders of magnitude. Such a decrease in concentration
315 of nucleated particles results from the limiting effect of \sqrt{L} on monomer concentration. If pre-existing particles are
316 absent, then no major loss mechanisms for monomers exist prior to the nucleation burst. Monomer would accumulate
317 until the nucleation energy barrier can be overcome: the higher the energy barrier, the higher the monomer
318 concentration prior to nucleation, as shown in Fig. 2c. The elevated monomer concentration then leads to rapid growth
319 of freshly nucleated particles immediately following the nucleation burst. However, in the presence of pre-existing
320 particles (i.e., $\sqrt{L} \neq 0$), monomer concentration can only increase to the point where its production and consumption
321 by preexisting particles reach balance, prohibiting its concentration from reaching a high value even prior to the

322 nucleation burst. To facilitate comparison with experimental results, in Appendix B we provide an example of
323 conversion from dimensionless distributions and growth rates to dimensional ones.

324 Finally, Fig. 5 examines the difference between representative sizes used to calculate GR_m when loss to preexisting
325 particles is accounted for. Two cases are presented: (1) collision-controlled nucleation ($E=0$) with $\sqrt{L} = 0.2$ (Fig. 5a-
326 5c) and (2) nucleation accounting for both cluster evaporation and scavenging by preexisting particles ($E =$
327 1×10^{-3} and $\sqrt{L} = 0.2$; Fig. 5d-5f). For collision-controlled nucleation with $\sqrt{L} = 0.2$, the preexisting particles
328 changes nucleation only slightly, although GR_m decreases and GR_{true}/GR_m increases both to a minor extent compared
329 to collision-controlled nucleation in the absence of a preexisting aerosol (compare Fig. 5a-5c to Fig. 3a-3c). The
330 analysis made in the discussion of Fig. 3a-3c still stands for Fig. 5a-5c. For nucleation with evaporation and preexisting
331 particles coupled together (Fig. 5d-5f), three features are worthy of attention. Firstly, compared to evaporation-only
332 nucleation, GR_m is significantly decreased for small particle sizes. For $\tilde{d}_p < 10$, GR_m is no larger than 0.7 with
333 preexisting particles but can be greater than 1.5 without (refer to Fig. 3e). Secondly, as shown in Fig. 5f, $GR_{true}/GR_{m,sr50}$
334 and $GR_{true}/GR_{m,tot50}$ come close to unity due to negligible coagulation effects. Third, $GR_{true}/GR_{m,mode}$ is between 1.2 and
335 1.5 and $GR_{true}/GR_{m,sr100}$ is between 1.1 and 1.2 for $\tilde{d}_p > 10$, indicating the true growth will be slightly underestimated
336 if $\tilde{d}_{p,mode}$ or $\tilde{d}_{p,sr100}$ are used to infer GR_{true} .

337 **3.4 Underestimation of GR_{true}**

338 In previous sections, mainly overestimation of the GR_{true} by measured growth rate, GR_m , has been discussed. Though
339 we do no quantitatively study underestimation of GR_{true} by GR_m , in this section we show that in a constant rate system
340 where particle sink processes (i.e. dilution and loss to pre-existing particles) strongly decrease the concentration of
341 nucleated particles, GR_m can approach zero and cannot be utilized to estimate GR_{true} . Figure 6 shows such nucleation
342 scenarios for (a) collision-controlled nucleation with $M = 0.1$ and (b) collision-controlled nucleation with $\sqrt{L} = 1.5$.
343 In both cases other sink processes were set equal to zero. As shown in both Fig. 6a and 6b, particle size distributions
344 approach steady state after $\tau = 100$. As a result, the measured growth rate GR_m approaches zero beyond $\tau = 100$. At
345 the same time, true condensational growth remains finite since monomer concentration remains steady state after $\tau =$
346 20. Therefore, other methods have to be utilized to infer GR_{true} in such situations.

347

348 **4 Conclusions**

349 We used a discrete-sectional model to solve a dimensionless form of aerosol population balance equation for a single-
350 species system. True growth rate and various “measured” growth rates were examined for a variety of nucleation
351 scenarios. Based on the simulation results, we draw the following conclusions:

352 1. Simulated data shows that for collision-controlled nucleation without preexisting particles, growth rates
353 inferred from the modal size of nucleated particles ($GR_{m,mode}$) is as much as 6 times greater than true growth
354 rates due to vapor condensation (GR_{true}).

355 2. In the absence of preexisting particles or other sink processes, comparison of different growth rates based on
356 different representative sizes indicates the relationship $GR_{m,mode} < GR_{m,sr100} < GR_{m,tot50} < GR_{m,sr50}$ holds true for
357 collision-controlled nucleation. If clusters evaporate, the nucleation process is characterized by rapid particle
358 growth following the nucleation burst.

359 3. Both evaporation and scavenging by preexisting particles can reduce the concentration of particles formed
360 by nucleation. Lower particle concentrations reduce the effect of coagulation on GR_m , so overestimation of
361 GR_{true} by GR_m is lower than is found in the absence of these processes.

362 4. Preexisting particles have dramatically different effects on collision-controlled nucleation and nucleation
363 with cluster evaporation. For $\sqrt{L} \in [0,0.3]$, collision-controlled nucleation is only slightly affected. However,
364 if preexisting particles are coupled with evaporation, the number of nucleated particles can drop significantly,
365 thus reducing the contribution of coagulation to measure growth rates.

366 5. GR_m can underestimate GR_{true} in a system with strong dilution or other particle sink processes. Particle size
367 distributions in such nucleation scenarios can approach a steady state that leads to a GR_m close to 0, which
368 underestimates GR_{true} .

369 **Appendix A**

370 To evaluate the contribution of self-coagulation of the mode ($GR_{m, self}$) and cluster coagulation ($GR_{m, cluster}$) to
 371 measured growth rate based on mode diameter ($GR_{m, mode}$), we used the following first order numerical approximation
 372 method:

- 373 1. Find particle size distribution $\tilde{n} = \tilde{n}(k, \tau)$ at a given time τ . k is the number of monomers in a particle and \tilde{n}_k
 374 is the concentration of particles that contains k molecules. Since the simulation code only reports discrete particle
 375 concentration for each bin, an interpolation is performed using Matlab function *griddedInterpolant.m*.
- 376 2. Find the value $k = k_{max}$ at which $3 \log(10) k \tilde{n}(k, \tau)$ is locally maximized. A prefactor $3 \log(10) k$ is
 377 multiplied to $\tilde{n}(k, \tau)$ to convert the particle size distribution to $d\tilde{N}/d\log_{10} \tilde{d}_p$. The mode diameter is then given
 378 by $\tilde{d}_{p, mode}(\tau) = \left(\frac{6k_{max}}{\pi}\right)^{1/3}$
- 379 3. Use the following integration equations to obtain number distribution of the mode at time $\tau + \Delta\tau$ assuming only
 380 one process causes the distribution to shift.

381 For self-coagulation:

$$382 \tilde{n}_{self}(k, \tau + \Delta\tau) = \tilde{n}(k) + 0.5 * \Delta\tau * \int_L^k c(x, k - x) \tilde{n}(x, \tau) \tilde{n}(k - x, \tau) dx - \int_L^H c(x, k) \tilde{n}(k, \tau) \tilde{n}(x, \tau) dx. \quad (A1)$$

383 For coagulation with clusters:

$$384 \tilde{n}_{cluster}(k, \tau + \Delta\tau) = \tilde{n}(k, \tau) + 0.5 \cdot \Delta\tau \cdot \int_{L_c}^{H_c} c(x, k - x) \tilde{n}(x, \tau) \tilde{n}(k - x, \tau) H(H_c - k + x) dx + \Delta\tau \cdot \\ 385 \int_{L_c}^{H_c} c(x, k - x) \tilde{n}(x, \tau) \tilde{n}(k - x, \tau) H(k - x - H_c) dx - \Delta\tau \cdot \int_{L_c}^{H_c} c(x, k) \tilde{n}(x, \tau) \tilde{n}(k, \tau) dx. \quad (A2)$$

386 In the above equations, L and H are the lower and upper boundary of the mode, L_c and H_c are the lower and
 387 upper boundary of clusters, $c(i, j)$ is the collision frequency function, $H(x)$ is the Heaviside step function. $\Delta\tau$ is
 388 typically set between 0.1 to 1.

- 389 4. Find the k values at which $3 \log(10) k \tilde{n}_{self}(k, \tau + \Delta\tau)$ and $3 \log(10) k \tilde{n}_{cluster}(k, \tau + \Delta\tau)$ are locally
 390 maximized. The corresponding diameters are $\tilde{d}_{p, self}(\tau + \Delta\tau)$ and $\tilde{d}_{p, cluster}(\tau + \Delta\tau)$.
- 391 5. The growth rate due to self-coagulation and coagulation with clusters are then given by

$$392 GR_{m, self} = \frac{\tilde{d}_{p, self}(\tau + \Delta\tau) - \tilde{d}_{p, mode}(\tau)}{\Delta\tau}; GR_{m, cluster} = \frac{\tilde{d}_{p, cluster}(\tau + \Delta\tau) - \tilde{d}_{p, mode}(\tau)}{\Delta\tau}. \quad (A3)$$

393 **Appendix B**

394

395 To facilitate comparison between dimensionless simulation results and experimental results, or previous dimensional
396 simulation results, we convert selected dimensionless simulation results to dimensional quantities using Eq. (6).
397 Specifically, we assume the monomer production rate is $R = 1 \times 10^6 \text{ cm}^{-3} \text{ s}^{-1}$ and the monomer has a volume of
398 $1.62 \times 10^{-22} \text{ cm}^3$ and a density of 1.47 g cm^{-3} . The collision frequency function for monomers, $\beta_{11, fm}$, is
399 $4.27 \times 10^{-10} \text{ cm}^3 \text{ s}^{-1}$, calculated at atmospheric pressure and 300 K. We consider two nucleation scenarios. The first
400 is collision-controlled nucleation in the presence of pre-existing particles, with \sqrt{L} set to 0.2. The second scenario is
401 nucleation with evaporation in the presence of pre-existing particles. The evaporation constant in this case is $E =$
402 1×10^{-3} and \sqrt{L} is 0.2. Both these cases are discussed in Sect. 3.3. The converted dimensional results are shown in
403 Fig. B1, with relevant dimensional quantities displayed in the figure.

404 **Acknowledgements**

405 This research was supported by the US Department of Energy's Atmospheric System Research, an Office of Science,
406 Office of Biological and Environmental Research program, under grant number DE-SC0011780.

407 **Nomenclature**

408 Collision-controlled nucleation: a limiting case for nucleation where all collisions between condensing (nucleating)
409 vapor occur at the rate predicted by kinetic theory and particles stick with 100% efficiency. Vapor does not
410 subsequently evaporate from particle surfaces, nor are particles scavenged by pre-existing particles or the chamber
411 wall

412 $\tilde{d}_{p,min}$: particle size corresponding to the local minimum in a $d\tilde{N}/d\log_{10}\tilde{d}_p$ representation of particle size distribution

413 $\tilde{d}_{p,mode}$: particle size corresponding to the local maximum in a $d\tilde{N}/d\log_{10}\tilde{d}_p$ representation of particle size
414 distribution

415 $\tilde{d}_{p,sr50}$: particle size of a measurement bin where particle concentration reaches 50% of its maximum value

416 $\tilde{d}_{p,sr100}$: particle size of a measurement bin where particle concentration reaches maximum value

417 $\tilde{d}_{p,tot50}$: particle size above which total particle concentration reaches 50% of its maximum value

418 $GR_{m,mode}$: measured dimensionless growth rate based on $\tilde{d}_{p,mode}$

419 $GR_{m,sr50}$: measured dimensionless growth rate based on $\tilde{d}_{p,sr50}$

420 $GR_{m,sr100}$: measured dimensionless growth rate based on $\tilde{d}_{p,sr100}$

421 $GR_{m,tot50}$: measured dimensionless growth rate based on $\tilde{d}_{p,tot50}$

422 GR_{true} : true dimensionless particle growth rate attributed to the net flux of condensing vapors onto particle surface
423 (i.e., the condensation rate minus the evaporation rate)

424 $GR_{m,clsuter}$: measured dimensionless particle growth rate attributed to coagulation with clusters
425 $GR_{m,self}$: measured dimensionless growth rate attributed to self-coagulation of particles in the nucleation mode
426 E, Ω : dimensionless parameters characterizing evaporation rates of particles, derived from the liquid droplet model.
427 E can be regarded as a dimensionless form of saturation vapor pressure of the condensing molecules and Ω a
428 dimensionless form of surface tension. Ω assumes a constant value of 16 in this work.
429 \sqrt{L} : dimensionless parameter characterizing fractional loss rate of monomer or nucleated particles to pre-existing
430 particles
431 \tilde{N}_k : dimensionless concentration of particles containing k monomers (i.e., k molecules of condensed vapor)

432 **References**

433 Almeida, J., Schobesberger, S., Kürten, A., Ortega, I. K., Kupiainen-Määttä, O., Praplan, A. P., Adamov, A.,
434 Amorim, A., Bianchi, F., Breitenlechner, M., David, A., Dommen, J., Donahue, N. M., Downard, A., Dunne,
435 E., Duplissy, J., Ehrhart, S., Flagan, R. C., Franchin, A., Guida, R., Hakala, J., Hansel, A., Heinritzi, M.,
436 Henschel, H., Jokinen, T., Junninen, H., Kajos, M., Kangasluoma, J., Keskinen, H., Kupc, A., Kurtén, T.,
437 Kvashin, A. N., Laaksonen, A., Lehtipalo, K., Leiminger, M., Leppä, J., Loukonen, V., Makhmutov, V.,
438 Mathot, S., McGrath, M. J., Nieminen, T., Olenius, T., Onnela, A., Petäjä, T., Riccobono, F., Riipinen, I.,
439 Rissanen, M., Rondo, L., Ruuskanen, T., Santos, F. D., Sarnela, N., Schallhart, S., Schnitzhofer, R., Seinfeld,
440 J. H., Simon, M., Sipilä, M., Stozhkov, Y., Stratmann, F., Tomé, A., Tröstl, J., Tsagkogeorgas, G.,
441 Vaattovaara, P., Viisanen, Y., Virtanen, A., Vrtala, A., Wagner, P. E., Weingartner, E., Wex, H., Williamson,
442 C., Wimmer, D., Ye, P., Yli-Juuti, T., Carslaw, K. S., Kulmala, M., Curtius, J., Baltensperger, U., Worsnop, D.
443 R., Vehkamäki, H., and Kirkby, J.: Molecular understanding of sulphuric acid–amine particle nucleation in
444 the atmosphere, *Nature*, 502, 359, 10.1038/nature12663
445 <https://www.nature.com/articles/nature12663-supplementary-information>, 2013.
446 Barsanti, K. C., McMurry, P. H., and Smith, J. N.: The potential contribution of organic salts to new
447 particle growth, *Atmos. Chem. Phys.*, 9, 2949–2957, 10.5194/acp-9-2949-2009, 2009.
448 Chan, T. W., and Mozurkewich, M.: Measurement of the coagulation rate constant for sulfuric acid
449 particles as a function of particle size using tandem differential mobility analysis, *Journal of Aerosol
450 Science*, 32, 321–339, [https://doi.org/10.1016/S0021-8502\(00\)00081-1](https://doi.org/10.1016/S0021-8502(00)00081-1), 2001.
451 Friedlander, S. K.: *Smoke, dust, and haze : fundamentals of aerosol dynamics*, 2nd ed.. ed., New York :
452 Oxford University Press, New York, 2000.
453 Fuchs, N. A., and Sutugin, A. G.: HIGH-DISPersed AEROSOLS A2 - HIDY, G.M, in: *Topics in Current
454 Aerosol Research*, edited by: Brock, J. R., Pergamon, 1, 1971.
455 Gelbard, F., and Seinfeld, J. H.: The general dynamic equation for aerosols. Theory and application to
456 aerosol formation and growth, *Journal of Colloid and Interface Science*, 68, 363–382,
457 [https://doi.org/10.1016/0021-9797\(79\)90289-3](https://doi.org/10.1016/0021-9797(79)90289-3), 1979.
458 Gelbard, F., and Seinfeld, J. H.: Simulation of multicomponent aerosol dynamics, *Journal of Colloid and
459 Interface Science*, 78, 485–501, [https://doi.org/10.1016/0021-9797\(80\)90587-1](https://doi.org/10.1016/0021-9797(80)90587-1), 1980.
460 Heisler, S. L., and Friedlander, S. K.: Gas-to-particle conversion in photochemical smog: Aerosol growth
461 laws and mechanisms for organics, *Atmospheric Environment* (1967), 11, 157–168,
462 [https://doi.org/10.1016/0004-6981\(77\)90220-7](https://doi.org/10.1016/0004-6981(77)90220-7), 1977.

463 Hodshire, A. L., Lawler, M. J., Zhao, J., Ortega, J., Jen, C., Yli-Juuti, T., Brewer, J. F., Kodros, J. K., Barsanti,
464 K. C., Hanson, D. R., McMurry, P. H., Smith, J. N., and Pierce, J. R.: Multiple new-particle growth
465 pathways observed at the US DOE Southern Great Plains field site, *Atmos. Chem. Phys.*, 16, 9321-9348,
466 10.5194/acp-16-9321-2016, 2016.
467 Kerminen, V. M., and Kulmala, M.: Analytical formulae connecting the "real" and the "apparent"
468 nucleation rate and the nuclei number concentration for atmospheric nucleation events, *Journal of*
469 *Aerosol Science*, 33, 609-622, 2002.
470 Kontkanen, J., Olenius, T., Lehtipalo, K., Vehkamäki, H., Kulmala, M., and Lehtinen, K. E. J.: Growth of
471 atmospheric clusters involving cluster–cluster collisions: comparison of different growth rate methods,
472 *Atmos. Chem. Phys.*, 16, 5545-5560, 10.5194/acp-16-5545-2016, 2016.
473 Kuang, C., Riipinen, I., Yli-Juuti, T., Kulmala, M., McCormick, A. V., and McMurry, P. H.: An improved
474 criterion for new particle formation in diverse atmospheric environments, *Atmospheric Chemistry and*
475 *Physics*, 10, 1-12, 10.5194/acp-10-1-2010, 2010.
476 Kuang, C., Chen, M., Zhao, J., Smith, J., McMurry, P. H., and Wang, J.: Size and time-resolved growth rate
477 measurements of 1 to 5 nm freshly formed atmospheric nuclei, *Atmos. Chem. Phys.*, 12, 3573-3589,
478 10.5194/acp-12-3573-2012, 2012.
479 Kulmala, M., Petäjä, T., Nieminen, T., Sipilä, M., Manninen, H. E., Lehtipalo, K., Dal Maso, M., Aalto, P. P.,
480 Junninen, H., Paasonen, P., Riipinen, I., Lehtinen, K. E. J., Laaksonen, A., and Kerminen, V.-M.:
481 Measurement of the nucleation of atmospheric aerosol particles, *Nature Protocols*, 7, 1651,
482 10.1038/nprot.2012.091
483 <https://www.nature.com/articles/nprot.2012.091-supplementary-information>, 2012.
484 Kürten, A., Li, C., Bianchi, F., Curtius, J., Dias, A., Donahue, N. M., Duplissy, J., Flagan, R. C., Hakala, J.,
485 Jokinen, T., Kirkby, J., Kulmala, M., Laaksonen, A., Lehtipalo, K., Makhmutov, V., Onnela, A., Rissanen, M.
486 P., Simon, M., Sipilä, M., Stozhkov, Y., Tröstl, J., Ye, P., and McMurry, P. H.: New particle formation in the
487 sulfuric acid–dimethylamine–water system: reevaluation of CLOUD chamber measurements and
488 comparison to an aerosol nucleation and growth model, *Atmos. Chem. Phys.*, 18, 845-863, 10.5194/acp-
489 18-845-2018, 2018.
490 Lehtinen, K. E. J., and Kulmala, M.: A model for particle formation and growth in the atmosphere with
491 molecular resolution in size, *Atmos. Chem. Phys.*, 3, 251-257, 10.5194/acp-3-251-2003, 2003.
492 Lehtinen, K. E. J., Rannik, U., Petaja, T., Kulmala, M., and Hari, P.: Nucleation rate and vapor
493 concentration estimations using a least squares aerosol dynamics method - art. no. D21209, *Journal of*
494 *Geophysical Research-Atmospheres*, 109, 21209, 2004.
495 Lehtipalo, K., Rondo, L., Kontkanen, J., Schobesberger, S., Jokinen, T., Sarnela, N., Kürten, A., Ehrhart, S.,
496 Franchin, A., Nieminen, T., Riccobono, F., Sipilä, M., Yli-Juuti, T., Duplissy, J., Adamov, A., Ahlm, L.,
497 Almeida, J., Amorim, A., Bianchi, F., Breitenlechner, M., Dommen, J., Downard, A. J., Dunne, E. M.,
498 Flagan, R. C., Guida, R., Hakala, J., Hansel, A., Jud, W., Kangasluoma, J., Kerminen, V.-M., Keskinen, H.,
499 Kim, J., Kirkby, J., Kupc, A., Kupiainen-Määttä, O., Laaksonen, A., Lawler, M. J., Leiminger, M., Mathot, S.,
500 Olenius, T., Ortega, I. K., Onnela, A., Petäjä, u., Praplan, A., Rissanen, M. P., Ruuskanen, T., Santos, F. D.,
501 Schallhart, S., Schnitzhofer, R., Simon, M., Smith, J. N., Tröstl, J., Tsagkogeorgas, G., Tome, A. n.,
502 Vaattovaara, P., Hanna Vehkama ki1, Vrtala, A. E., Wagner, P. E., Williamson, C., Wimmer, D., Winkler,
503 P. M., Virtanen, A., Donahue, N. M., Carslaw, K. S., Baltensperger, U., Riipinen, I., Curtius, J., Worsnop, D.
504 R., and Kulmala, M.: The effect of acid-base clustering and ions on the growth of atmospheric nano-
505 particles, *Nature Communications*, 7, 11594, 2016.
506 Lehtipalo , K., Leppa , J , Kontkanen , J , Kangasluoma , J , Franchin , A , Wimnner , D , Schobesberger , S ,
507 Junninen , H , Petaja , T , Sipila , M , Mikkila , J , Vanhanen , J , Worsnop , D R & Kulmala: Methods for
508 determining particle size distribution and growth rates between 1 and 3 nm using the Particle Size
509 Magnifier, *Boreal Environment Research*, 19, 215-236, 2014.

510 McMurry, P. H., and Friedlander, S. K.: New particle formation in the presence of an aerosol, *Atmos.*
511 *Environ.*, 13, 1635-1651, 1979.

512 McMurry, P. H.: Photochemical aerosol formation from SO₂: A theoretical analysis of smog chamber
513 data, *Journal of Colloid and Interface Science*, 78, 513-527, [https://doi.org/10.1016/0021-9797\(80\)90589-5](https://doi.org/10.1016/0021-9797(80)90589-5), 1980.

514 McMurry, P. H., and Wilson, J. C.: Growth laws for the formation of secondary ambient aerosols:
515 Implications for chemical conversion mechanisms, *Atmospheric Environment* (1967), 16, 121-134,
516 [https://doi.org/10.1016/0004-6981\(82\)90319-5](https://doi.org/10.1016/0004-6981(82)90319-5), 1982.

517 McMurry, P. H., and Li, C.: The dynamic behavior of nucleating aerosols in constant reaction rate
518 systems: Dimensional analysis and generic numerical solutions, *Aerosol Science and Technology*, 51,
519 1057-1070, 10.1080/02786826.2017.1331292, 2017.

520 Olenius, T., Riipinen, I., Lehtipalo, K., and Vehkamäki, H.: Growth rates of atmospheric molecular clusters
521 based on appearance times and collision–evaporation fluxes: Growth by monomers, *Journal of Aerosol*
522 *Science*, 78, 55-70, <https://doi.org/10.1016/j.jaerosci.2014.08.008>, 2014.

523 Pichelstorfer, L., Stolzenburg, D., Ortega, J., Karl, T., Kokkola, H., Laakso, A., Lehtinen, K. E. J., Smith, J. N.,
524 McMurry, P. H., and Winkler, P. M.: Resolving nanoparticle growth mechanisms from size- and time-
525 dependent growth rate analysis, *Atmos. Chem. Phys. Discuss.*, 2017, 1-24, 10.5194/acp-2017-658, 2017.

526 Rao, N. P., and McMurry, P. H.: Nucleation and Growth of Aerosol in Chemically Reacting Systems: A
527 Theoretical Study of the Near-Collision-Controlled Regime, *Aerosol Science and Technology*, 11, 120-
528 132, 10.1080/02786828908959305, 1989.

529 Riccobono, F.: Contribution of sulfuric acid and oxidized organic compounds to particle formation and
530 growth, *Atmos. Chem. Phys.*, 12, 9427-9439, 2012.

531 Riccobono, F.: Oxidation products of biogenic emissions contribute to nucleation of atmospheric
532 particles, *Science*, 344, 717-721, 2014.

533 Riipinen, I., Yli-Juuti, T., Pierce, J. R., Petäjä, T., Worsnop, D. R., Kulmala, M., and Donahue, N. M.: The
534 contribution of organics to atmospheric nanoparticle growth, *Nature Geoscience*, 5, 453,
535 10.1038/ngeo1499, 2012.

536 Smith, J., Dunn, M., VanReken, T., Iida, K., Stolzenburg, M., McMurry, P., and Huey, L.: Chemical
537 composition of atmospheric nanoparticles formed from nucleation in Tecamac, Mexico: Evidence for an
538 important role for organic species in nanoparticle growth, *Geophysical Research Letters*, 35, 2008.

539 Smith, J. N., Barsanti, K. C., Friedli, H. R., Ehn, M., Kulmala, M., Collins, D. R., Scheckman, J. H., Williams,
540 B. J., and McMurry, P. H.: Observations of aminium salts in atmospheric nanoparticles and possible
541 climatic implications, *Proceedings of the National Academy of Sciences*, 107, 6634-6639, 2010.

542 Stolzenburg, M. R., McMurry, P. H., Sakurai, H., Smith, J. N., Mauldin, R. L., Eisele, F. L., and Clement, C.
543 F.: Growth rates of freshly nucleated atmospheric particles in Atlanta, *Journal of Geophysical Research: Atmospheres*, 110, n/a-n/a, 10.1029/2005JD005935, 2005.

544 Tröstl, J., Chuang, W. K., Gordon, H., Heinritzi, M., Yan, C., Molteni, U., Ahlm, L., Frege, C., Bianchi, F.,
545 Wagner, R., Simon, M., Lehtipalo, K., Williamson, C., Craven, J. S., Duplissy, J., Adamov, A., Almeida, J.,
546 Bernhammer, A.-K., Breitenlechner, M., Brilke, S., Dias, A., Ehrhart, S., Flagan, R. C., Franchin, A., Fuchs,
547 C., Guida, R., Gysel, M., Hansel, A., Hoyle, C. R., Jokinen, T., Junninen, H., Kangasluoma, J., Keskinen, H.,
548 Kim, J., Krapf, M., Kürten, A., Laaksonen, A., Lawler, M., Leiminger, M., Mathot, S., Möhler, O., Nieminen,
549 T., Onnela, A., Petäjä, T., Piel, F. M., Miettinen, P., Rissanen, M. P., Rondo, L., Sarnela, N., Schobesberger,
550 S., Sengupta, K., Sipilä, M., Smith, J. N., Steiner, G., Tomè, A., Virtanen, A., Wagner, A. C., Weingartner,
551 E., Wimmer, D., Winkler, P. M., Ye, P., Carslaw, K. S., Curtius, J., Dommen, J., Kirkby, J., Kulmala, M.,
552 Riipinen, I., Worsnop, D. R., Donahue, N. M., and Baltensperger, U.: The role of low-volatility organic
553 compounds in initial particle growth in the atmosphere, *Nature*, 533, 527, 10.1038/nature18271, 2016.

554

555

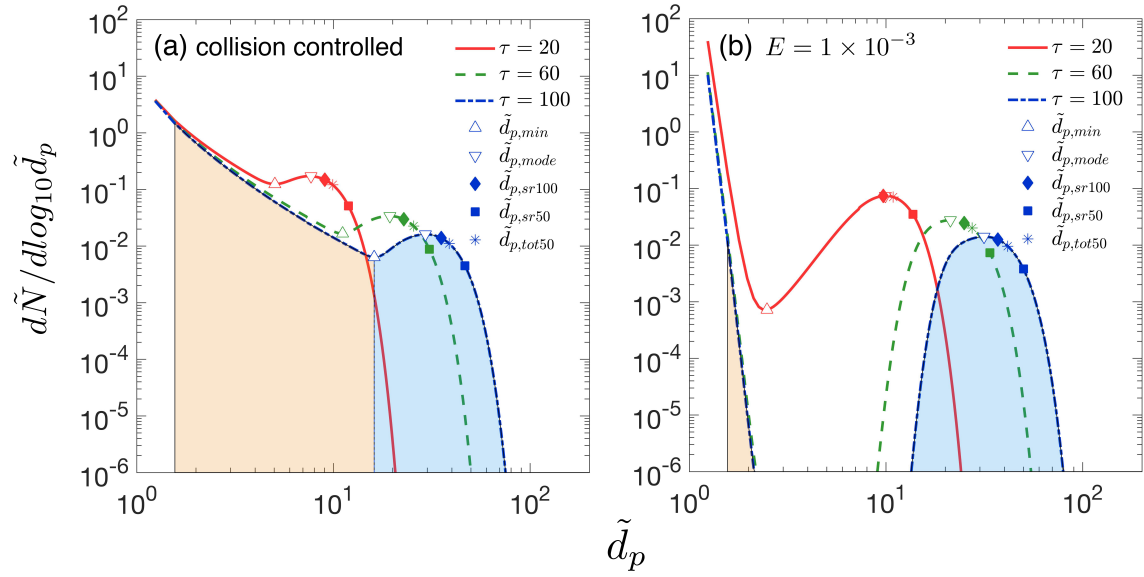
556 Verheggen, B., and Mozurkewich, M.: An inverse modeling procedure to determine particle growth and
557 nucleation rates from measured aerosol size distributions, *Atmospheric Chemistry and Physics*, 6, 2927-
558 2942, 2006.

559 Wang, J., McGraw, R. L., and Kuang, C.: Growth of atmospheric nano-particles by heterogeneous
560 nucleation of organic vapor, *Atmos. Chem. Phys.*, 13, 6523-6531, 10.5194/acp-13-6523-2013, 2013.

561 Weber, R. J., Marti, J. J., McMurry, P. H., Eisele, F. L., Tanner, D. J., and Jefferson, A.: Measurements of
562 new particle formation and ultrafine particle growth rates at a clean continental site, *Journal of
563 Geophysical Research: Atmospheres*, 102, 4375-4385, 10.1029/96JD03656, 1997.

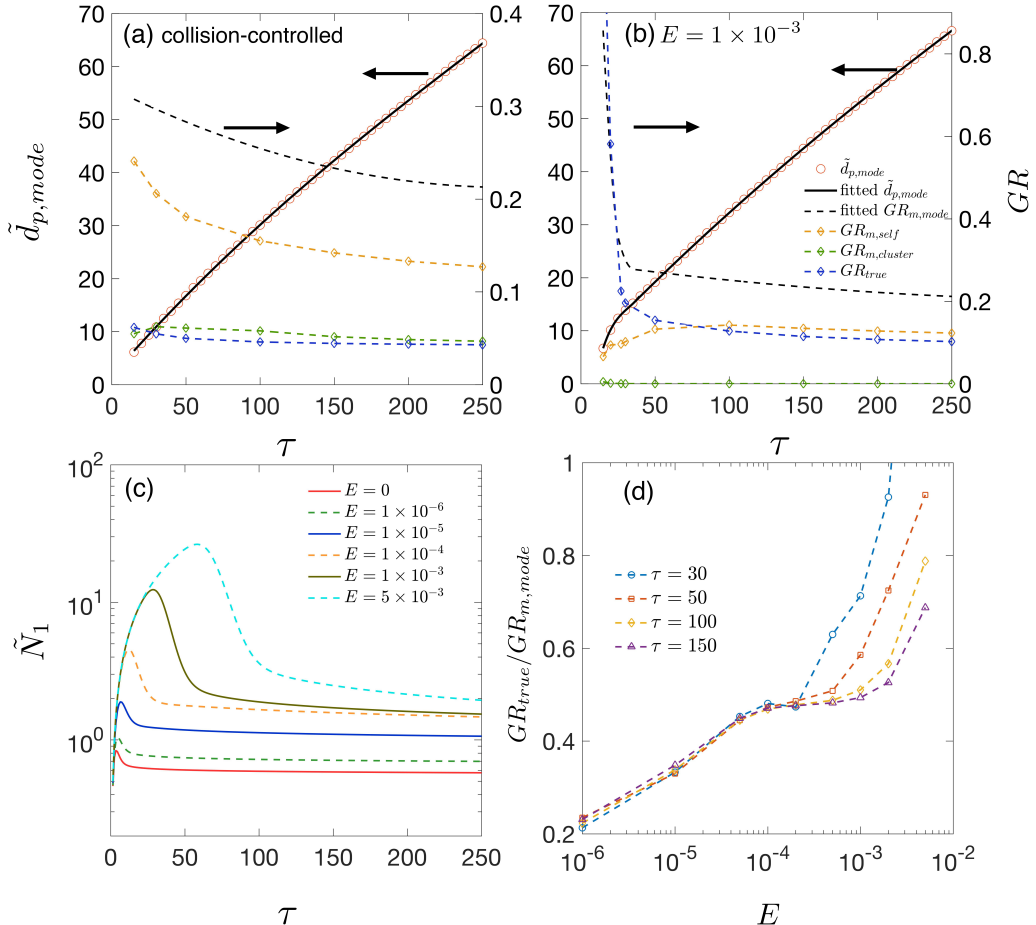
564 Yli-Juuti, T.: Growth rates of nucleation mode particles in Hyytiälä during 2003–2009: variation with
565 particle size, season, data analysis method and ambient conditions, *Atmos. Chem. Phys.*, 11, 12865-
566 12886, 2011.

567



568
569 **Figure 1.** Particle size distributions at dimensionless times $\tau = 20, 60, 100$ **(a)** for collision-controlled nucleation
570 ($E=0$) and **(b)** when evaporation is included with $E = 1 \times 10^{-3}$. Division of the distribution into monomer, cluster
571 and nucleation mode is displayed for $\tau = 100$, with beige and light blue indicating the range of clusters and nucleation
572 mode. Clusters and nucleation mode are separated by $\tilde{d}_{p,min}$, where $d\tilde{N}/d\log_{10}\tilde{d}_p$ is at a local minimum.
573 Characteristic sizes $\tilde{d}_{p,mode}$, $\tilde{d}_{p,sr100}$, $\tilde{d}_{p,sr50}$ and $\tilde{d}_{p,tot50}$ are marked for each time. The relationship between
574 symbols and characteristic sizes is shown only for $\tau=100$.

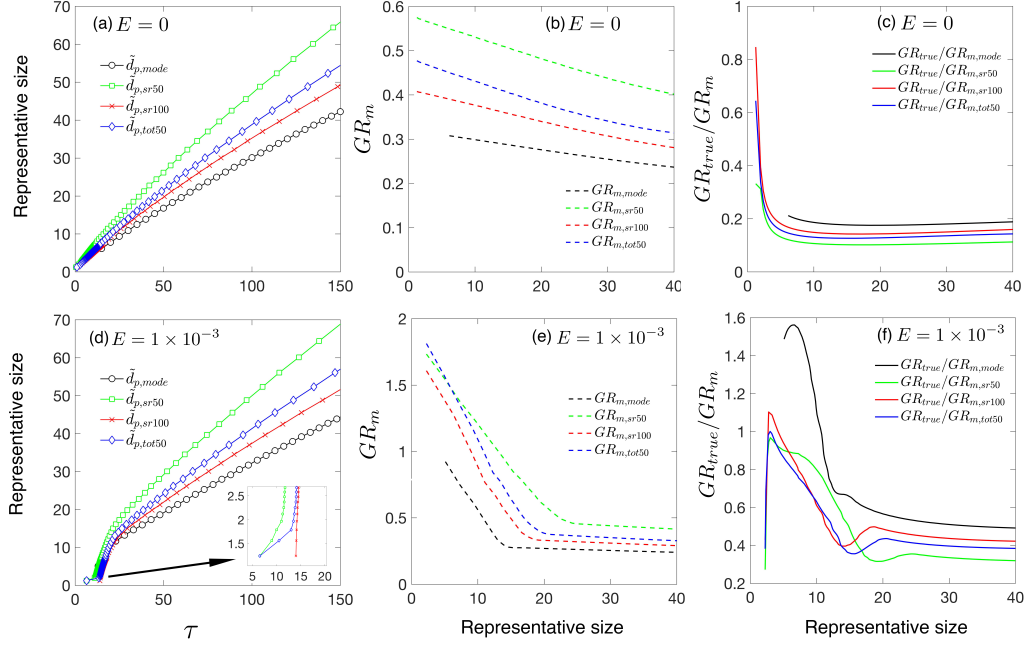
575



576

577 **Figure 2. (a)** $\tilde{d}_{p,mode}$ and various growth rates as functions of time for collision-controlled nucleation. Dashed black
 578 lines show the value of $GR_{m,mode}$. Yellow, green and blue dashed lines represent $GR_{m,self}$, $GR_{m,cluster}$ and GR_{true}
 579 respectively. **(b)** The same quantities as are shown in (a) but with the evaporation constant set to $E = 1 \times 10^{-3}$. For
 580 both Fig. 2a and 2b, the left axis shows value for the solid lines and the right axis shows values for the dashed lines.
 581 **(c)** Monomer concentration as functions of time for different values of E . **(d)** $GR_{true}/GR_{m,mode}$ for different values of E
 582 at $\tau = 30, 50, 100, 150$.

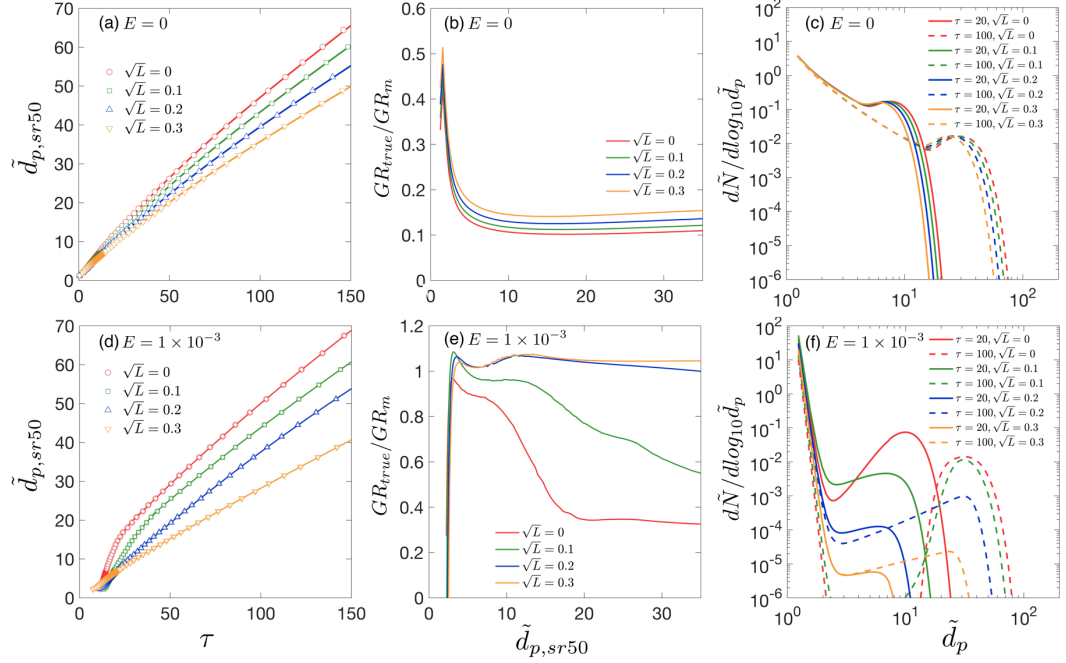
583



584

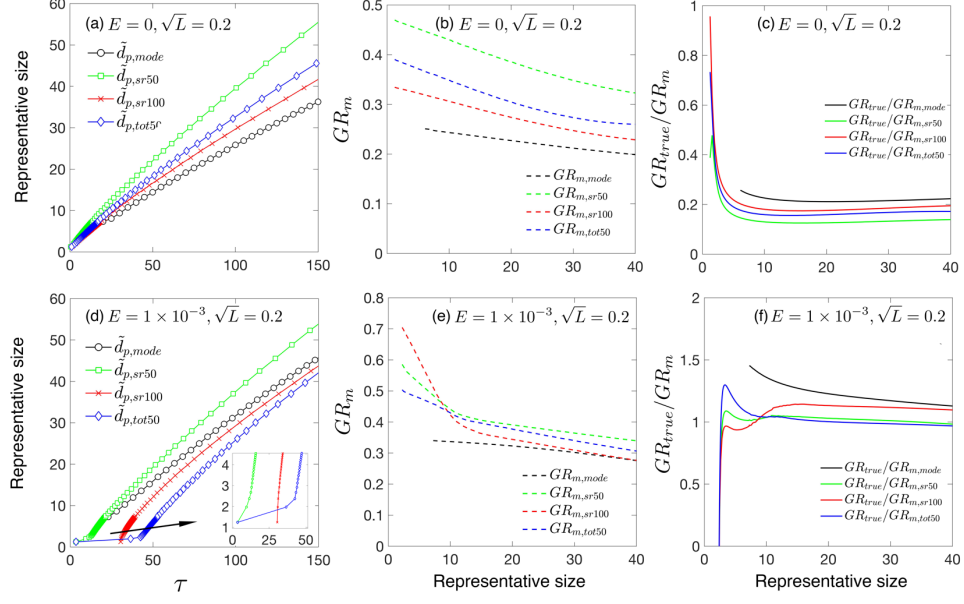
585 **Figure 3.** (a) $\tilde{d}_{p,mode}$, $\tilde{d}_{p,sr100}$, $\tilde{d}_{p,tot50}$, $\tilde{d}_{p,bin50}$ as functions of time. (b) Measured growth rates $GR_{m,mode}$, $GR_{m,sr50}$,
 586 $GR_{m,sr100}$, $GR_{m,tot50}$ as functions of representative sizes. (c) Ratio of true growth rate to measured growth rate,
 587 GR_{true}/GR_m . Figures 3a-3c are for collision-controlled nucleation with $E=0$. Figures 3d-3f show the same quantities
 588 as are shown in Fig. 3a-3c but with $E = 1 \times 10^{-3}$.

589



590
591 **Figure 4.** Effect of preexisting particles on particle growth rate. **(a)** $\tilde{d}_{p,sr50}$ as a function of time. **(b)** Ratio of true
592 growth rate to measured growth rate, $GR_{true}/GR_{m,sr50}$. **(c)** Particle size distributions at $\tau = 20$ and $\tau = 100$. Figures
593 4a-4c are for collision-controlled nucleation with $E = 0$ and $\sqrt{L} = 0, 0.1, 0.2, 0.3$. Figures 4c-4d show the same
594 quantities as are shown in Fig. 4a-4c but with $E = 1 \times 10^{-3}$.

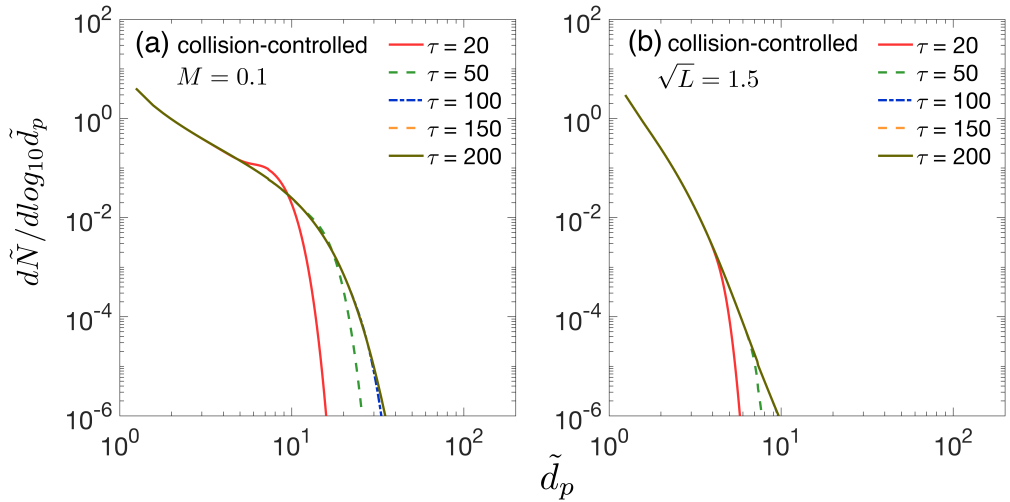
595



596

597 **Figure 5.** (a) $\tilde{d}_{p,mode}$, $\tilde{d}_{p,sr100}$, $\tilde{d}_{p,tot50}$, $\tilde{d}_{p,bin50}$ as functions of time. (b) Measured growth rate $GR_{m,mode}$, $GR_{m,sr50}$,
598 $GR_{m,sr100}$, $GR_{m,tot50}$ as functions of representative sizes. (c) Ratio of true growth rate to measured growth rate,
599 GR_{true}/GR_m . Figures 5a-5c are for collision-controlled nucleation with $E = 0$ and $\sqrt{L} = 0.2$. Figures 5d-5f show the
600 same quantities as are shown in Fig. 5a-5c but with $E = 1 \times 10^{-3}$.

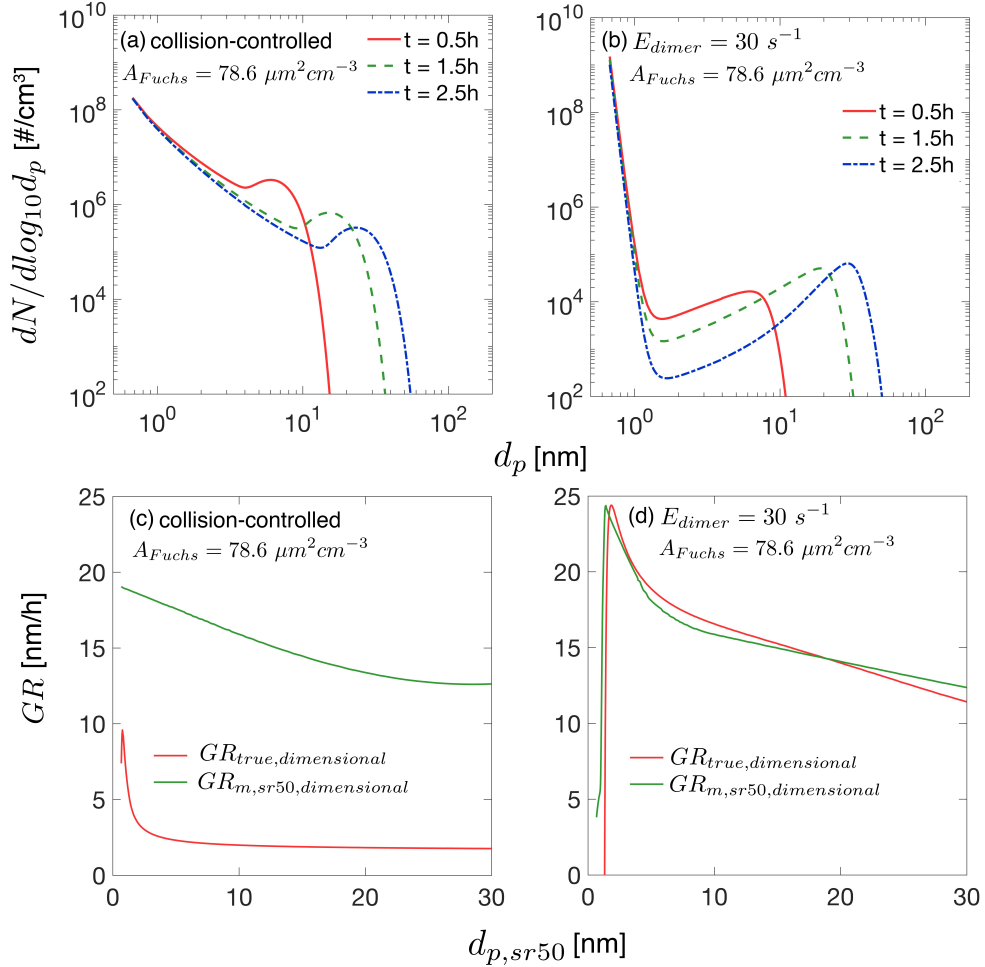
601



602

603 **Figure 6.** Particle size distribution at different dimensionless times for collision-controlled nucleation with **(a)** $M=0.1$
 604 and **(b)** $\sqrt{L} = 1.5$. In both cases, sink processes not indicated in the figure were set to zero in the simulations. Particle
 605 size distributions at certain times are not visible in the figure since they overlap with the particle size distribution at a
 606 later time.

607



610 **Figure B1.** Dimensional particle size distribution and growth rates. The quantities shown in this figure are converted
 611 from the dimensionless solution using Eqn. (6). The dimensional quantities involved in the conversions are $R =$
 612 $1 \times 10^6 \text{ cm}^{-3} \text{ s}^{-1}$, $\beta_{11, fm} = 4.27 \times 10^{-10} \text{ cm}^3 \text{ s}^{-1}$ and $v_1 = 1.62 \times 10^{-22} \text{ cm}^3$. The Fuchs surface area is 78.6
 613 $\mu\text{m}^2 \text{ cm}^{-3}$, corresponding to $\sqrt{L}=0.2$. **(a)** Particle size distribution for collision controlled nucleation at $t = 0.5\text{h}$, 1.5h and 2.5h . **(b)** Particle size distribution for nucleation with evaporation at $t = 0.5\text{h}$, 1.5h and 2.5h . Monomer evaporation
 614 rate from dimer is 30 s^{-1} , corresponding to a dimensionless evaporation constant $E = 1 \times 10^{-3}$. **(c)** The dimensional
 615 particle growth rates for collision-controlled nucleation as is shown in Fig. B1a. **(d)** The dimensional particle growth
 616 rates for nucleation with evaporation as is shown in Fig. B1b.